Studies on Positioning Manipulators Actuated by Solid Media Transmissions

Haoran Zhao[1], Xin Liu[2], Rahul Korpu[4], Michael J. Heffernan[3], Aaron T. Becker[1], and Nikolaos V. Tsekos[2]

Abstract—**Fluidic transmission mechanisms use fluids to transmit force through conduits. We previously presented a transmission mechanism called solid-media transmission (SMT), which uses conduits filled with spheres and spacers for push-only bidirectional transmission. In this paper, we present new designs of SMT-actuated one-degree-of-freedom (DoF) and two-degree-of-freedom positioning manipulators, and report experiment studies to assess their performance. In these studies, closed-loop position control was performed with a PI controller and/or master-slave control. With braided PTFE tubing, SMT exhibited sub-millimeter accuracy, with a tolerance of $\pm 0.05\,\mathrm{mm}$ for the tested transmission lines with lengths up to $4\,\mathrm{m}$.**

I. INTRODUCTION

Over centuries engineers, mechanics, and scientists have introduced, modified, and optimized myriad versions of mechanical transmission systems. Example transmissions include cables, belts, driveshafts, mechanical linkages, and fluidic power transmission systems [1]–[7]. Many of these designs were a triumph of engineering innovation optimized for a particular domain or application, however each transmission mechanism offers benefits and drawbacks.

Within this context, we previously described a transmission mechanism called solid media transmission (SMT) [8]–[10]. SMT uses conduits filled with a force-transmitting medium and the conduits can be curved to route transmission. Figure 1 shows a one-DoF, SMT-actuated linear manipulator mounted on a UR3 robot arm. Similar to hydraulic hoses, the robot arm is being used as a fixed support, to demonstrate that the SMT lines can be flexibly routed. The SMT force transmission medium is composed of repetitive elemental units. The units are spheres as in Fig. 2(a) and (c) or pairs of spheres and spacers as in Fig. 2(b) and (d). As illustrated in Fig. 2, the SMT components form a solid backbone, transversely self-adjustable to fit into its channels. The original motivation for SMT was to actuate manipulators inside magnetic resonance imaging (MRI) scanners for performing interventions [8], [9], [11]. From the mechanical aspect, those studies demonstrated sufficient kinematic performance and MR compatibility. The piston-free SMT system offers high flexibility in developing scalable and

[1]Dept. of Electrical and Computer Engineering, University of Houston, Houston, USA zhaohaorandl@gmail.com
[2]Dept. of Computer science, University of Houston, Houston, USA nvtsekos@central.uh.edu
[3]GuidaBot, LLC., Houston, USA michael@fannininnovation.com
[4]Dept. of Mechanical Engineering, University of Houston, Houston, USA
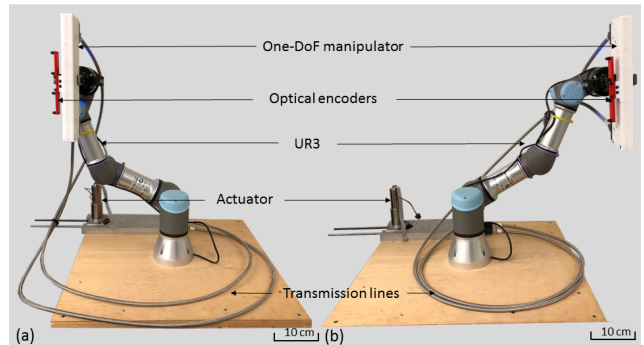
Fig. 1. One-DoF manipulator actuated by solid-media transmission mounted on UR3 robot arm. The flexible transmission lines follow the movement of the robot arm from left-side to right-side.

compact manipulators. These early works, combined with a description of SMT-based force amplifiers and multi-port manifolds [10], support the notion that secondary to its leak-free, fluid-less yet fluidic-like nature SMT may have merit as an alternative transmission mechanism for other domains. The purpose of this paper is to present one and two-degree-of-freedom positioning manipulator designs, and validate the hypothesis proposed in [12], that materials and dimensions dominate performance, on a one-degree-of-freedom manipulator with different combinations of spheres and conduits. Benchtop experimental studies focused on proportional-integral (PI) control of our one-DoF manipulator and master-slave control for our manipulator with two SMT-actuated DoF. The paper is organized as follows: Section II describes the mechanical design of our one and two-DoF manipulators. Sections III and IV provide the kinematic and configuration space descriptions. Section V presents the experiment studies of material selection on our one-DoF manipulator, and two-DoF manipulator positioning control with a pair of $2\,\mathrm{m}$ transmission conduits. Finally, we discuss and outline future work in Section VI. And video demo is shown on YouTube as [13].

II. MECHANICAL DESIGN OF TWO SMT-ACTUATED MANIPULATORS

A. One-DoF SMT-Actuated Linear Manipulator

Our one-DoF, SMT-actuated, linear manipulator is described in Fig. 3, which shows CAD perspectives and a photograph of the one-DoF manipulator that illustrate the
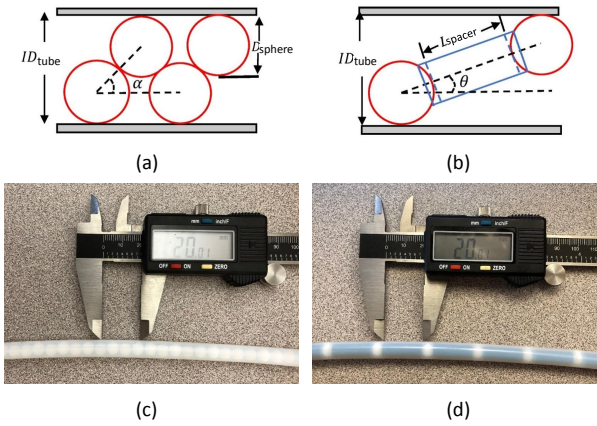
Fig. 2. Linear packing: (a) Illustration of SMT sphere packing (b) Illustration of SMT spacer and sphere packing (c) Experimental sphere zigzag packing (d) Experimental sphere and spacer zigzag packing. The spacers are hollow and the spheres fit partly inside. Where ID is inner diameter, D is diameter, and L is length.
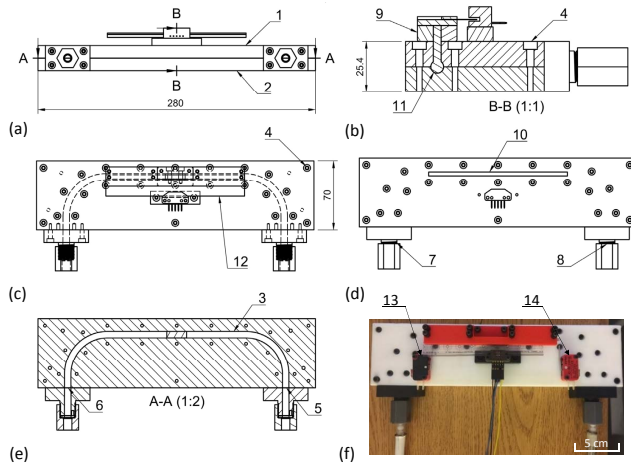

Fig. 3. End loop actuator (Fusion360 perspective drawing): (1) Upper layer (2) Bottom layer (3) Inner channel (4) Screw hole (5, 6) Channel ends (7, 8) Tubing fitting and adapter (9) Carriage (10) Slot (11) Piston (12) Optical encoder strip (13, 14) Stop switch.

primary practices devised and implemented in the design and prototyping of SMT actuated devices. The manipulator is composed of four CNC machined components: two matching layers (1) and (2) ($280\,\mathrm{mm} \times 70\,\mathrm{mm}$, made of Delrin), the half SMT channel (3), and a number of screw openings (4). When the two layers were screwed together the complete channel was formed with an $ID_\mathrm{channel} = 6.48\,\mathrm{mm}$, where ID means inner diameter. Two ends of the channel (5) and (6) were connected to the respective SMT tubing with custom-made connectors (7) and (8). The lumen transitions from $ID = 6.7\,\mathrm{mm}$ in the tubing to $ID = 6.48\,\mathrm{mm}$ in the channel. This transition takes place in the connector, in which the spheres of the SMT backbone move freely without any obstruction. The actuated unit is a carriage (9) which has a $20\,\mathrm{mm}$ slim extension that enters into the straight portion of the inner channel, via a slot (10) that was cut into upper layer (1). This $20\,\mathrm{mm}$ long extension serves as a piston
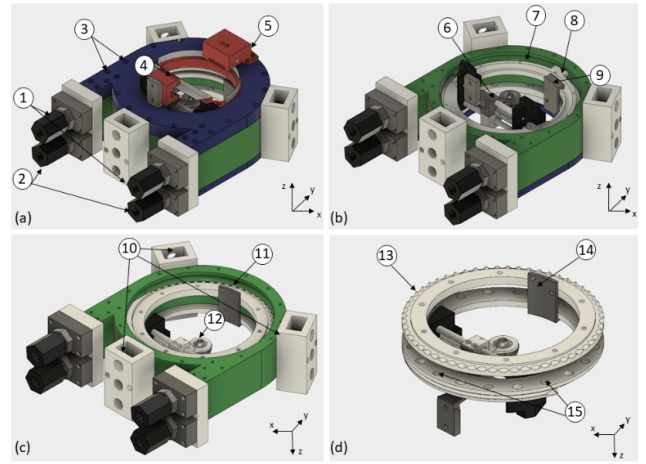

Fig. 4. RTS Fusion 360 3D schematics: (1, 2) SMT tubing connector (3) Screw opening (4) Optical encoder and strip for translation (5) Optical encoder and strip for rotation (6) Tool carriage (7) Inner channel of DoF-1 (rotation) (8) Inner block (9) Extended piston (10) Mount slot (11) Inner channel of DoF-2 (translation) (12) Ball-and-socket A (13) Sprocket (14) Bridge connection (15) Ball bearing. See video for an exploded drawing and animation.

(11): the distal-most SMT spheres impinging on its opposing sides push it bidirectionally. The carriage carries an optical encoder strip (12) (EM1 module, US Digital, Vancouver, WA). The carriage has a range of motion of $\pm 50\,\mathrm{mm}$, limited by switches (13) and (14). The signal of the optical encoder is fed to the cRIO for further processing.

B. Two-DoF SMT-Actuated Manipulator (RTS)

The two-DoF SMT-actuated robot Rotation-Translation-Stage (RTS) is described in Fig. 4, which shows the Fusion 360 schematics, and the photographs of the physical prototype model shown in Fig. 5. The RTS has two SMT-actuated DoF: a rotating ring, that sets DoF-1 (rotation angle $\alpha = \pm 90\,\mathrm{deg}$), and a prismatic translation, that sets DoF-2 (translational range $r = \pm 20\,\mathrm{mm}$). The inner SMT channels (7) and (11) with an $ID_\mathrm{channel} = 6.48\,\mathrm{mm}$, and a number of screw openings (3) were CNC machined. Two ends of the each DoF channel were connected to the respective SMT tubing with custom-made connectors (1) and (2). The lumen transitions are from $ID = 6.7\,\mathrm{mm}$ in the tubing to $ID = 6.48\,\mathrm{mm}$ in the two-DoF channel. This transition takes place in the connector, in which the spheres of the SMT backbone move freely without any obstruction. For DoF-1, the SMT pushes the block (8) inside the channel to change the rotation angle, also rotating a closed-loop track of spheres that control the translation angle. The optical strip and encoder (5) (EM1 module, US Digital, Vancouver, WA) are mounted to record the rotation displacement. Because the translation movement rotates with rotation input DoF-1, there is a bridge (14) with an extended piston (9) to connect the upper layer actuated by DoF-2 with the closed-loop track of spheres actuated by DoF-1. Actuation of DoF-2 moves the extended piston (9), which pushes the carriage (6) that carries a tool using the ball-and-socket A (12). An optical strip and encoder (4) mounted on the carriage record the linear displacement of
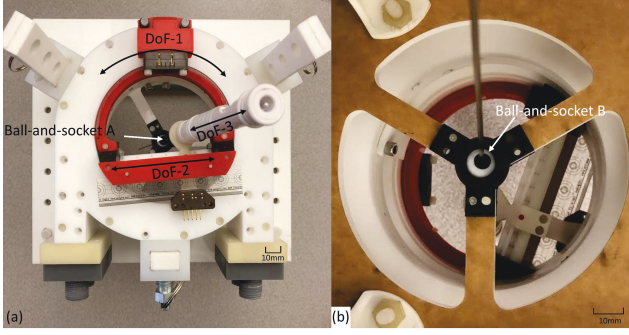
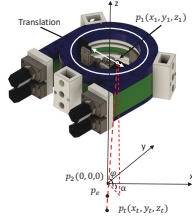Fig. 5.   Physical prototype model: (a) Top view (b) Bottom view.

Fig. 6.   CAD model of the RTS robot showing the coordinate frames for kinematic studies.

DoF-2. To improve the efficiency of DoF-2, which transfers force through the bridge, we utilize a sprocket design (13) instead of the smooth channel used for the rotation angle (7). Additionally, to reduce the resistance between layers of the channel while rotating, ball bearings were incorporated between layers (15). The RTS can be mounted using three slots (10) and spring-loaded latches. With the combined actuation of DoF-1 and DoF-2, the ball-and-socket A (12) can be positioned inside a circle of radius $\pm 20\,\mathrm{mm}$. The distal end of the tool is carried by ball-and-socket B, which is permanently anchored onto the frame of the robot. If a needle is placed between A and B, the tip of needle can be at any location (x_{tip},y_{tip},z_{tip}) of a spherical cone workspace.

III. RTS MANIPULATOR KINEMATICS

The RTS robot is not a serial kinematic chain, so to simplify the calculation of the forward kinematics, we used geometry and vector calculation rather than homogeneous transformation matrices. This analysis uses two stages RTS robots, rather than one stages RTS with a fixed ball-and-socket. We use subscripts to denote which stage is being referenced. Given the translation displacement T_1 and rotation angle α_1, the coordinate of the central ball-and-socket on the first layer stage is $P_1 = [x_1, y_1, z_1]^\top$. Given the translation displacement T_2 and rotation angle α_2, the coordinate of the central ball-and-socket on the second layer stage is $P_2 = (x_2, y_2, z_2)$. Because there is a separation s between the two stages (or one stage and a fixed ball-and-socket), we assume the needle has a minimum insertion depth $d_{\min}$, the range of insert depth d_{insert}, and maximum insertion depth

$d_{\mathrm{insert}} \in [0, d_{\max}]$. The needle entrance point P_e is:

$$\vec{P_e} = \vec{P_1} + d_{\min}\frac{\vec{P_1} - \vec{P_2}}{\|\vec{P_1} - \vec{P_2}\|_2} \tag{1}$$

and the target point P_t is:

$$\vec{P_t} = \vec{P_1} + (d_{\min} + d_{\mathrm{insert}})\frac{\vec{P_1} - \vec{P_2}}{\|\vec{P_1} - \vec{P_2}\|_2} \tag{2}$$

The RTS robot is abstracted as a torus (rotation), and a rod across the center of the torus (translation) as shown in Fig. 6. The experiment section uses only a single stage RTS, which means the coordinates of P_2 is $[0, 0, 0]^\top$, so the kinematics analysis is only based on the one stages RTS unite. The one stage RTS is driven by two pairs of SMT conduits, so the system inputs of two-DoF are two linear displacement inputs. For the rotation DoF-1, the rotational angle α_1 should be converted from displacement input as:

$$\alpha_1 = \frac{R}{2\pi r}2\pi = \frac{R}{r} \tag{3}$$

where R is rotation input, r is rotational radius, and the elevation angle φ:

$$\varphi = \arctan\left(\frac{T_1}{s}\right) \tag{4}$$

where T is translation input. With given information, the P_1 (x_1,y_1,z_1) is:

$$x_1 = T_1 \cos\alpha_1 \tag{5}$$
$$y_1 = T_1 \sin\alpha_1 \tag{6}$$

Where s is the separation distance of two stages, which is equal to z_1. And the target point with needle insertion length d_{insert}, the P_t is:

$$x_t = x_1 - (d_{\min} + d_{\mathrm{insert}}) \cos\varphi \sin\alpha_1 \tag{7}$$
$$y_t = y_1 - (d_{\min} + d_{\mathrm{insert}}) \cos\varphi \sin\alpha_1 \tag{8}$$
$$z_t = z_1 - (d_{\min} + d_{\mathrm{insert}}) \cos\varphi \sin\alpha_1 \tag{9}$$

Given a target position coordinate P_t, needle entrance position coordinate P_e, and needle insert length d_{insert}, the coordinates of two layers are calculated by substituting the givens to (1) and (2). The solutions are substituted into the following equations:

$$x = T \cos\alpha \tag{10}$$
$$y = T \sin\alpha \tag{11}$$
$$\alpha = \arctan\left(\frac{y}{x}\right) \tag{12}$$

To satisfy the range of DoF-1 and the symmetric design, the results of these calculations must satisfy the following constraints:

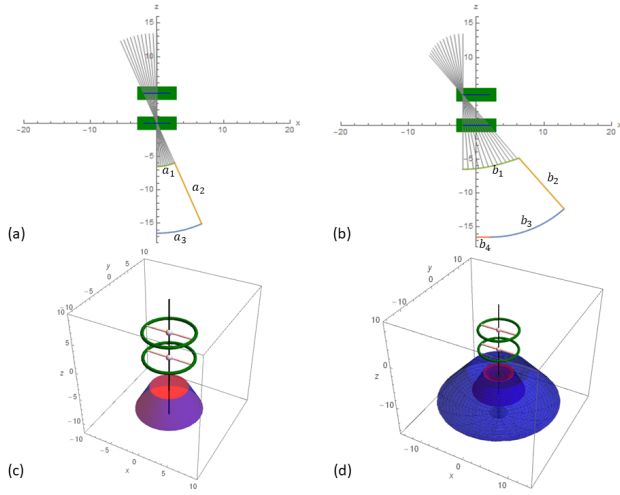$$\begin{cases} T = -|T| & x < 0 \\ T = |T| & 0 \le x \end{cases} \tag{13}$$

Fig. 7. The workspace generated by combining two stacked RTS robots. If the bottom manipulator is held constant, the workspace cross-section (a) is a sector of an annulus and the 3D workspace (b) is this workspace rotated about the z-axis. Allowing the bottom manipulator to move increases the workspace. The workspace cross-section (c) is a bounded by 4 arcs and the 3D workspace (d) is this workspace rotated about the z-axis.

IV. TWO-DOF MANIPULATOR CONFIGURATION SPACE

To better understand the characteristics of the RTS robot, this section investigates the robot configuration space, based on the previous kinematics calculations. The workspace of the RTS is a spherical cone, because of the symmetric design. The workspace is defined by a cross-section in the xz plane and revolved arcs about the z-axis. The cross-section in the xz plane is shown as Fig. 7 (a) and (b). In the Fig 7, the RTS is presented as a dark green rectangle as in Fig. 4. In the first case shown as Fig. 7 (a) and (c), there is only one stage RTS and the anchored ball-and-socket B (Fig. 5 (b)) is shown at the center of the lower layer stage. The cross-section of the configuration space consists of three arcs. In the all following equations, parameter $t \in [0,1]$. The function of the top arc $(x,z) = a_1(t)$ is:

$$x = d_{\min} \sin\left(\arctan\left(\frac{rt}{s}\right)\right) \tag{14}$$

$$z = -d_{\min} \cos\left(\arctan\left(\frac{rt}{s}\right)\right) \tag{15}$$

The function of the side slant $(x,z) = a_2(t)$ is given by:

$$x = (d_{\min} + td_{\max}) \sin\left(\arctan\left(\frac{rt}{s}\right)\right) \tag{16}$$

$$z = -(d_{\min} + td_{\max}) \cos\left(\arctan\left(\frac{rt}{s}\right)\right) \tag{17}$$

The function of the bottom arc $(x,z) = a_3(t)$ is:

$$x = (d_{\min} + d_{\max}) \sin\left(\arctan\left(\frac{rt}{s}\right)\right) \tag{18}$$

$$z = -(d_{\min} + d_{\max}) \cos\left(\arctan\left(\frac{rt}{s}\right)\right) \tag{19}$$
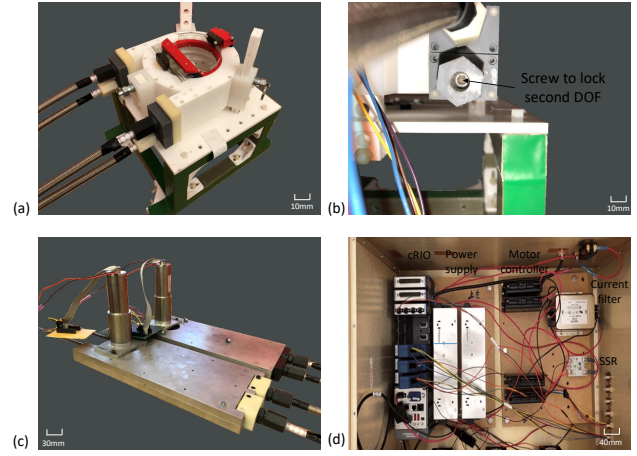

Fig. 8. Experiment setup: (a) Isometric view (b) One-DoF isolation case (c) Motor and motor base (d) Electronics box. From left to right are NI cRIO, power supplies×2, motor controllers×4, current filter and solid-state relay.

The second case, shown in Fig. 7 (b) and (d), uses two stacked RTS robots, and the cross-section of configuration space consists of four arcs. The function of the top arc $(x,z) = b_1(t)$ is:

$$x = 2r\left(t - \frac{1}{2}\right) + d_{\min} \sin\left(\arctan\left(\frac{2rt}{s}\right)\right) \tag{20}$$

$$z = -d_{\min} \cos\left(\arctan\left(\frac{2rt}{s}\right)\right) \tag{21}$$

The function of the side slant $(x,z) = b_2(t)$ is given by:

$$x = r + (d_{\min} + td_{\max}) \sin\left(\arctan\left(\frac{2rt}{s}\right)\right) \tag{22}$$

$$z = -(d_{\min} + td_{\max}) \cos\left(\arctan\left(\frac{2rt}{s}\right)\right) \tag{23}$$

The function of the bottom arc $(x,z) = b_3(t)$ is:

$$x = 2r\left(t - \frac{1}{2}\right) + (d_{\min} + d_{\max}) \sin\left(\arctan\left(\frac{2rt}{s}\right)\right) \tag{24}$$

$$z = -(d_{\min} + d_{\max}) \cos\left(\arctan\left(\frac{rt}{s}\right)\right) \tag{25}$$

and the function of the flat bottom side $(x,z) = b_4(t)$ is:

$$x = rt \tag{26}$$
$$z = -d_{\min} - d_{\max} \tag{27}$$

After revolving these arcs about the z-axis, the one and two RTS configuration spaces with anchored ball-and-socket B was plotted in Fig. 7 (c) and (d). Although this paper focuses on discussing a single RTS, using a second RTS stage extends the workspace, as shown in Fig. 7 (d). Two stacked RTS robots have a workspace nearly four times larger than a single stage.
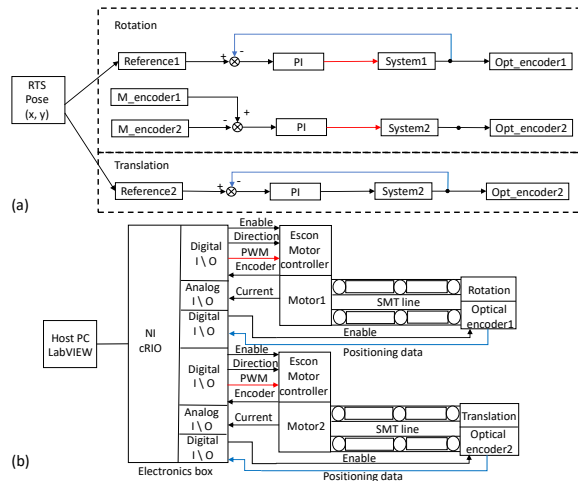
(a)

(b)

Fig. 9.   Two-DoF system diagram: (a) System control diagram (b) Signal flow diagram.

Fig. 10.   One-DoF experiment results: (a) The response time of $1\,\mathrm{m}$ transmission line with different material combinations (b) Experimental settling time for SMT with four lengths. Each box-and-whisker represents 10 trials.

V. EXPERIMENT STUDIES

All the experiments run until the manipulator settled within $0.05\,mm$ to the goals. The custom-made one-DoF positioning manipulator shown in Fig. 3 (f), and the two-DoF positioning manipulator presented in Fig. 8 (a) were bidirectionally actuated by a parallel pair of SMT lines. Each SMT pair was powered by a servo motor, as shown in Fig. 8 (c), driven by a control unit as shown in Fig. 8(d), and the control unit was a PC-based real-time controller (National Instrument Compact RIO (cRIO), NI Inc. Austin, USA). The experiment control and data measurement code were first developed in LabVIEW, then downloaded to cRIO for the drive motor and data acquisition. To drive the whole system, we customized, built, and tested a electronics box. The electronics box is powered by $120\,\mathrm{V}$ AC. Built-in safety features include a solid-state relay, fuse, switch and emergency button. The Maxon servo motor (Maxon DCX35L GB KL $24\,\mathrm{V}$, USA subsidiary) powers a dual rack and pinion (with a $43:1$ reduction ratio) to convert its rotational motion to linear by actuating two rods. These rods provide bidirectional actuation, with one rod for each SMT line. The system block diagram of the two-DoF manipulator is shown in 9 (b). The one-DoF manipulator system is similar, with only one transmission line pair.

The experimental studies of the RTS positioning accuracy and performance used two parallel pairs of braided PTFE tubing with an $ID = 6.7\,\mathrm{mm}$ and $OD = 8.3\,\mathrm{mm}$ (AFLEXHOSE, USA, LLC) as the transmission line, which has a stainless-steel jacket and PTFE inner tubing. Because the two-DoF of the RTS robot are dependent, we separated closed-loop performance tests into three cases. First, one of two-DoF was blocked by screws, as shown in Fig. 8 (b) and separately tested the accuracy of each degree-of-freedom. Second, two-DoF were connected with 2 parallel pairs of the transmission line, but only the corresponding motor was powered for each degree-of-freedom test. Third, two motors were powered as the input source for rotation, and one motor
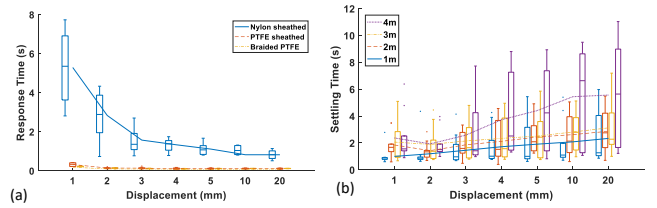
powered for translation. All above test of the one and two-DoF manipulators were implemented using PI controllers with hand-tuned gains. The closed-loop PI control diagram is similar to the Fig. 9 (a) translation section. The PI controller gains remained the same in all experiments for each experimental case. However, because the two-DoF of RTS are connected, to compensate and improve the performance of the system synchronization, we implemented a master-slave control (MS-control) strategy [14]. The output displacement of the rotation DoF-1 served as the displacement reference for the slave translation DoF-2. The master-slave closed-loop diagram for rotation is shown in the rotation section of Fig. 9 (A).

A. One-DoF Linear Manipulator Experiment Results

Prior works [9], [12], suggest that the three factors with the greatest impact on SMT performance are the friction between the tubing and solid media, tubing expansion, and conduit length. To improve system performance, we first analyzed the performance of materials with differing friction coefficients. Due to weight and shattering concerns, we experimented with nylon ($2-4\,\mathrm{GPa}$) and PTFE ($0.5\,\mathrm{GPa}$). Fortunately, the most common commercially available materials for tubing are nylon or PTFE. The friction coefficient of nylon to nylon is approximately 0.2, and the friction coefficient of PTFE to PTFE is approximately 0.04. We used $1\,\mathrm{m}$ long nylon and PTFE tubing with an $ID = 7\,\mathrm{mm}$ and an $OD = 9\,\mathrm{mm}$. Both the nylon tubing and the PTFE tubing were inserted into a UV-extruded acrylic tube ($ID = 9.35\,\mathrm{mm}$, $OD = 15\,\mathrm{mm}$). The external sheath was used to ensure the rigidity of the channel and prevent elastic deformation of tubing when the motor applies force and the solid media move. The acrylic sheathes were zip-tied to an aluminum frame to ensure the tubing run was straight. While the acrylic sheathes limited deformation, there still was $0.35\,\mathrm{mm}$ clearance between the outer wall of tubing and the inner wall of the sheath. We also used $1\,\mathrm{m}$ braided PTFE tubing with an $ID = 6.7\,\mathrm{mm}$ and $OD = 8.3\,\mathrm{mm}$ (AFLEXHOSE, USA, LLC), which has a stainless-steel jacket and PTFE inner tubing. In experiments to compare the performance of conduit length, we used the braided PTFE tubing in lengths up to $4\,\mathrm{m}$.

For friction comparison experiments, we used step functions as the input reference signal, whose magnitudes were 1, 2, 3, 4, 5, 10, and $20\,\mathrm{mm}$. Figure 10 shows experiment results using box plots and each box-and-whisker represents
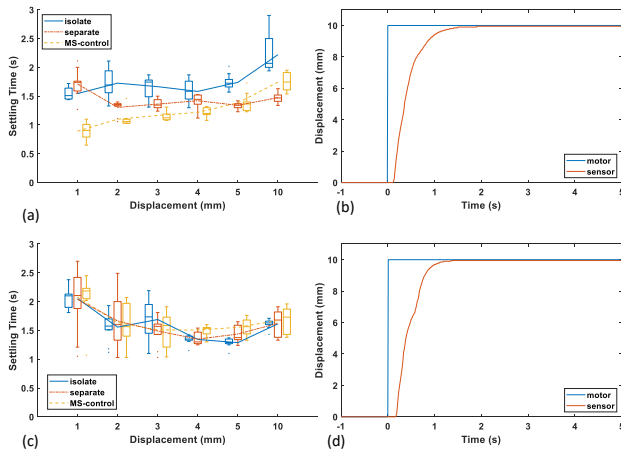
Fig. 11. Two-DoF manipulator experiment results: (a) The settling time of rotation, (b) representative MS-control result for rotation, (c) the settling time of translation, (d) representative MS-control result for translation.

10 randomized direction trials. As Fig. 10 (a) shows, the average response time with nylon tubing and nylon spheres enclosed in an acrylic sheath is $1.97\,\mathrm{s}$. Switching to PTFE spheres and tubing reduced the average response time to $0.15\,\mathrm{s}$. To improve performance by further limiting tubing expansion, we used a PTFE stainless-steel braided tubing and PTFE spheres. The new setup shrinks the average response time to $0.1\,\mathrm{s}$, which means PTFE has better performance than nylon. Next, we investigated the performance of different transmission conduit lengths from $1\,\mathrm{m}$ to $4\,\mathrm{m}$. Fig. 10 (b) shows that the settling time increases with length from $1.76\,\mathrm{s}$ for $1\,\mathrm{m}$ to $4.12\,\mathrm{s}$ for $4\,\mathrm{m}$. Despite this, the position accuracy for all length and material experiments always reached the resolution of the optical encoder which was $0.05\,\mathrm{mm}$. Our system with the new one-DoF manipulator design and PTFE braided conduit has a response time that is twice as fast, and a settling time that is 10 times faster than our previous system in [12].

B. Two-DoF Manipulator Experiment Results

For the two-DoF closed-loop positioning control studies, we separately investigated three cases (*isolate*, *separate*, and *MS-control*). We used step functions as the input reference signal, whose magnitudes were 1, 2, 3, 4, 5, and $10\,\mathrm{mm}$. Each set was repeated 10 times with randomized direction for all experiments. Fig. 11 (a) shows the rotation (DoF-1) settling time results. Two optical recorders with $0.05\,\mathrm{mm}$ resolution were used to record displacement. The settling time of the *isolate* case is higher than the others and shows an uptrend from $1.5\,\mathrm{s}$ to $2.2\,\mathrm{s}$. Because the two-DoF of RTS are dependent, when we used a screw to block one DoF, the solid media in the RTS and conduits were highly compressed which caused high resistance. So as the input step magnitude increased, the settling time increased. The settling time of the separate case is from $1.7\,\mathrm{s}$ to $1.4\,\mathrm{s}$. These results confirm phenomenon in our previous work [9], [12], that the resistance forces weaken the input force, and reduce the level of system sensitivity, so the settling time is high if

the system input is small. With four transmission conduits connected, the settling time of the *separate* case is less than the *isolate* case, but also has the same compression problem. The master-slave control method compensated for the two motor synchronization problem and reduced the compression of the solid media. As the input magnitude increased, the settling time increased, and the settling time is from $0.8\,\mathrm{s}$ to $1.6\,\mathrm{s}$, which has better performance than the *separate* or *isolate* cases.

The settling time of translation (DoF-2) is shown in Fig. 11 (c). Because of the compression problem mentioned before, the measured settling time for the *isolate* case is unpredictable, and in the range from $0.8\,\mathrm{s}$ to $1.9\,\mathrm{s}$. For the *separate* and *MS-control* cases, DoF-2 is controlled by the PI controller, so they have similar plots, and the settling time is from $1.5\,\mathrm{s}$ to $2.5\,\mathrm{s}$. The reason for this slight difference is because that when DoF-1 changes, the inner packing pattern of the solid media changes unpredictably, which reduces SMT performance. Figure 11 (c) and (d) show responses of bidirectional step input result of the system, and for all trials the system accuracy reached the resolution of the optical encoder ($0.05\,\mathrm{mm}$).

VI. CONCLUSIONS

We are at an early stage of understanding the SMT mechanism and assessing its potential and means for implementing it. The data presented herein illustrated that closed-loop SMT can quickly and accurately respond to a reference signal. Additionally, the error for lengths from 1 to $4\,\mathrm{m}$ can be regulated within the resolution of a $0.05\,\mathrm{mm}$ optical encoder. From the system studies we concluded that the experiment results on our one-DoF manipulator verified the hypothesis of four primary factors (friction, length, expansion, and mechanical design) proposed in our previous work [12]. We also presented and analyzed an SMT-actuated two-DoF manipulator design and its closed-loop positioning control performance. Because of the high nonlinear characteristics presented in the experiment results, in the future we will focus on system identification to achieve better control results, and will optimize the mechanical design of SMT-based manipulators.

REFERENCES

[1] V. Agrawal, W. J. Peine, and B. Yao, "Modeling of transmission characteristics across a cable-conduit system," *IEEE Transactions on Robotics*, vol. 26, no. 5, pp. 914–924, 2010.

[2] G. Palli, G. Borghesan, and C. Melchiorri, "Modeling, identification, and control of tendon-based actuation systems," *IEEE Transactions on Robotics*, vol. 28, no. 2, pp. 277–290, 2012.

[3] R. Dhaouadi, K. Kubo, and M. Tobise, "Two-degree-of-freedom robust speed controller for high-performance rolling mill drives," *IEEE transactions on industry applications*, vol. 29, no. 5, pp. 919–926, 1993.

[4] H. Elliott, T. Depkovich, J. Kelly, and B. Draper, "Nonlinear adaptive control of mechanical linkage systems with application to robotics," in *American Control Conference, 1983*. IEEE, 1983, pp. 1050–1055.

[5] D. McCloy and H. R. Martin, "Control of fluid power: analysis and design," *Chichester, Sussex, England, Ellis Horwood, Ltd.; New York, Halsted Press, 1980. 505 p.*, 1980.

[6] R. S. Hartenberg and J. Denavit, *Kinematic synthesis of linkages*. McGraw-Hill, 1964.

[7] A. Salimi, A. Ramezanifar, J. Mohammadpour, and K. Grigoriadis, "Gain-scheduling control of a cable-driven MRI-compatible robotic platform for intracardiac interventions," in *American Control Conference (ACC), 2013*. IEEE, 2013, pp. 746–751.

[8] N. C. von Sternberg, J. An, K. Chin, D. J. Shah, and N. V. Tsekos, "A new method for MR compatible actuation: Solid media flexible transmission," Joint Annual Meeting ISMRM-ESMRMB 2014, Milan, Italy, 2014.

[9] X. Liu, D. Biediger, R. Korpu, E. G. Christoforou, and N. V. Tsekos, "A new transmission mechanism for the actuation of manipulators for magnetic resonance imaging (MRI) guided interventions," in *XIV Mediterranean Conference on Medical and Biological Engineering and Computing 2016*. Springer, 2016, pp. 673–678.

[10] L. Huang, X. Liu, N. V. Tsekos, and A. T. Becker, "Two missing components for solid media transmission: Amplifiers and manifolds," in *Automation Science and Engineering (CASE), International Conference on*. IEEE, 2016, pp. 207–212.

[11] N. V. Tsekos and M. J. Heffernan, "Robotic device for image-guided surgery and interventions," Greek and German Patent US20 170 135 772A1, May 18, 2017, US Patent App. 15/402,135. [Online]. Available: https://patents.google.com/patent/US20170135772A1/en

[12] H. Zhao, X. Liu, H. M. Zaid, D. J. Shah, M. J. Heffernan, A. T. Becker, and N. V. Tsekos, "Early studies of a transmission mechanism for mr-guided interventions," in *Bioinformatics and Bioengineering (BIBE), 2017 IEEE 17th International Conference on*. IEEE, 2017, pp. 450–456.

[13] H. Zhao. (2019) Studies on positioning manipulators actuated by solid media transmissions. [Online]. Available: https://www.youtube.com/watch?v=Os5KGcmPqcs&feature=youtu.be

[14] F. J. Perez-Pinal, C. Nunez, R. Alvarez, and I. Cervantes, "Comparison of multi-motor synchronization techniques," in *IEEE Industial Electronics Society. Annual conference*, 2004.